The Ball-on-Three-Balls strength test for discs and plates: Extending and simplifying stress evaluation

Maximilian Staudacher [*], Tanja Lube, Peter Supancic

Department of Materials Science, Montanuniversität Leoben, Franz Josef-Strasse 18, A-8700 Leoben, Austria

ABSTRACT

The Ball-on-Three-Balls-test has proven to be an accurate and easy-to-use option for strength testing. However, the maximum stress must be calculated based on Finite-Element-Analysis results. For this purpose, a fitted function was already provided. This function is based on results which were generated under the assumption of punctiform load introduction. Deviations from these conditions occur through an increase in contact-area between the loading ball and the specimen, large specimen deformations, friction, or plastic deformation of the balls. These non-linear effects are investigated by Finite-Element-Analysis for a wide range of specimens. It is shown that the maximum stress is sensitive to the area of contact between the loading ball and the specimen. Furthermore, thin specimens are subject to large deformations, which significantly decrease the maximum stress. Therefore, a revised fitted function is derived. For specimens with exceptional geometries, non-linear effects are considered with correction factors added to the new fitted function.

1. Introduction

Strength testing is probably the most important tool for ceramic material characterization and material development. It allows the determination of both general mechanical strength and the scatter thereof, which then enables the prediction and reduction of component failure [1]. Today, a number of mechanical testing methods are widely available and well examined. They can be categorized by the type of stress field that the specimen is subjected to, which is usually either uniaxial or biaxial. The main uniaxial testing methods are 3-or 4-point-bending, tensile and compression tests [2,3]. Biaxial testing methods can be classified by the symmetry of their stress distribution, being either axisymmetric or not. Examples for common methods with axisymmetric stress distributions are the Ring-on-Ring-test (RoR), the Ball-on-Ring-test or the Ball-with-flat-on-Ring-test [4–6]. Common methods employing non-axisymmetric stress distributions are the Ball-on-Three-Balls-test (B3B), the Piston-on-Three-Balls-test (P3B), the Ball-on-Ring-of-Balls-test and the Three-Balls-on-Three-Balls-test [7–12]. A significant disadvantage of axisymmetric tests is that a high degree of flatness of the specimen is required in order to guarantee even contact throughout the ring. This results in either additional specimen preparation requirements or deviations from the ideal analytical stress field due to uneven load distribution [13,14]. Therefore, tests utilizing a support of three balls have been

developed since non-planar discs can still be stably supported. The Piston-on-Three-Balls-test shows a similar problem, since the surface beneath the punch has to be planar to ensure uniform load application – the condition that has been assumed to derive the equation for the stress calculation. Furthermore, with increasing deformation of the sample, the assumption of an extended area of uniform pressure is lost and load application shifts towards the outer edge of the piston. This leaves testing methods such as the Ball-on-Three-Balls-test as one of the most tolerant to non-planar specimens and most flexible in terms of specimen geometry. As a result, it is among the most common biaxial testing methods and is employed for a variety of materials [15–24]. An extensive study about the influence of the most important sources of error has been conducted by Börger et al. [25]. Furthermore, the strongly localized area of maximum stress allows testing of specific regions of a component to generate spatially resolved strength results [26]. A prerequisite for an accurate evaluation for all tests that use an analytical stress calculation is to perform them under conditions of small deflections and linear elastic material behavior, i.e. maintaining a linear stress-deflection relationship. This is assured by prescribing that the support radius is smaller than about 6–20 times the specimen thickness [4,13,20]. Taking into account that manufacturing tolerances make support rings smaller than 5 mm in radius impractical [13], the lower limit for the thickness of strong specimens is approximately 0.5 mm in the RoR-test. The B3B-test, however, can easily
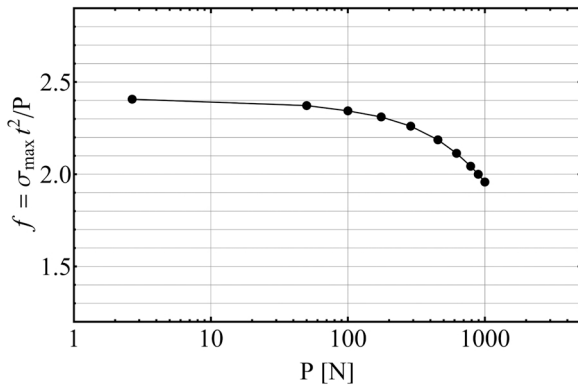

Fig. 1. FEA-results for the factor *f* in dependence of the applied load *P* for an exemplary specimen with a radius of 12 mm, a support radius of 10 mm and a thickness *t* of 1 mm. The specimen's Young's modulus and Poisson's ratio are 70 GPa and 0.22, respectively.

Fig. 3. Meshed Model 2 with a punctiform load *P* applied.

be scaled down to much smaller support radii. With the use of standardized bearing balls, specimens as small as $2 \times 2 \times 0.13$ mm^3 have been tested successfully [27–29]. However, the main disadvantage of the B3B-test is that no sufficiently accurate analytical description of the full stress field is available and numerical analysis has to be employed to determine the maximum stress and the effective volume or surface for each specimen [30,31]. This then entails new difficulties in making those results available. One possibility is to provide fitting functions for the factor *f*, which relates the applied load and the maximum tensile stress, as has been done by Börger et al. [30]. Yet, these functions are cumbersome to use and only provide a solution for the ideal case of punctiform load introduction and small deformations. Deviations from these ideal conditions lead to a load dependency of the factor *f*, as shown for an exemplary specimen in Fig. 1, which is not represented in [30]. This may lead to a significant overestimation of the specimen's strength [32].

Within this work, a new expression for the ideal case of both discs and square plate specimens will be derived by utilizing FEA for linear elastic isotropic materials. By modifying the range and variables of the underlying data field, a new and simpler fit with similar accuracy to the one derived by Börger et al. [30] will be presented. Furthermore, the difference between the ideal case and real testing situations, such as an increase in contact-area between the loading ball and the specimen, large specimen deformations, friction, or plastic deformation of the loading ball will be discussed. The effect of large specimen deformations will be investigated by utilizing a combined analytical and numerical approach. The effect of an increasing contact-area at the loading ball will be examined by utilizing FEA. This will yield correction factors which describe the load-dependency of the factor *f*. The performance of
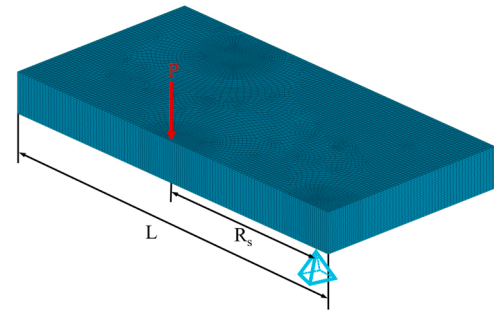
this new evaluation and its corrections will be assessed by comparison with an elaborate FEA model. The practical aspects given by the new evaluation and its valid domain of application will be discussed.

2. Methods

2.1. Finite-Element-Analysis

FEA was performed to generate grid points for fitting and to investigate specific effects. All simulations were conducted utilizing the commercial FEA-program ANSYS R21.1 (ANSYS Inc., PA 15317, Canonsburg, USA). Each of the following models was implemented as a script written in Ansys-Parametric-Design-Language (APDL). This allowed using them in automated parametric studies for a wide range of geometries and isotropic material properties, covering several thousand unique combinations.

2.1.1. Simplified models for discs

To investigate the dependence of the factor *f* on the testing geometry as well as the specimen's elastic properties, the 3D-model shown in Fig. 2a) was utilized. Due to the symmetry of the system and loading conditions, the model could be reduced to one sixth of the full disc. In Model 1A, the loading ball was represented by a punctiform load applied in the center of the disc. The support ball was represented by a punctiform boundary condition at the support radius R_s. Consequently, this model represents the ideal case during testing. The specimen was meshed with 178958 SOLID95 elements (20-node brick elements) and 749574 nodes. The script further facilitates the implementation of various types of load application in the center of the specimen. To examine the influence of a finite area of contact, a Hertzian contact-pressure distribution with varying extent was utilized in Model 1B, as depicted in Fig. 2b).
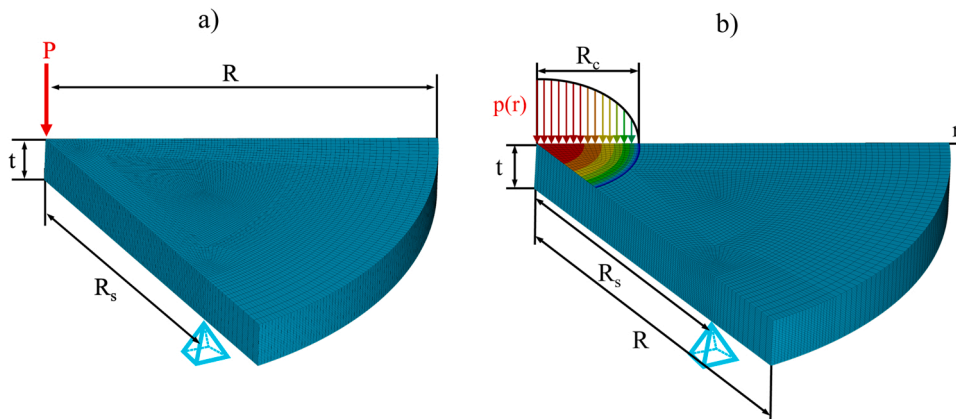
Fig. 2. a) displays the meshed Model 1A with a punctiform load *P* applied. b) shows Model 1B, but with a Hertzian contact-pressure distribution *p(r)* applied.
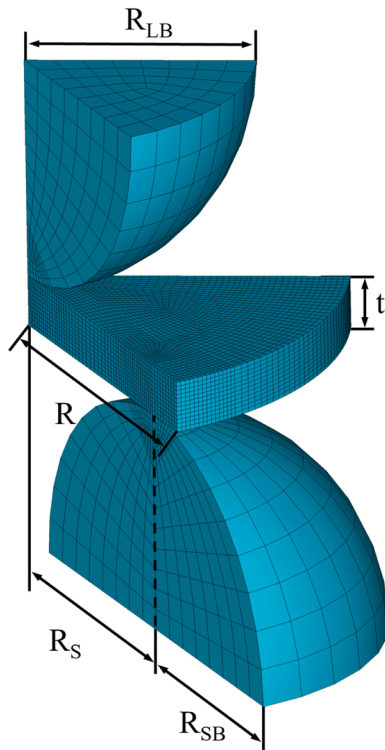
Fig. 4. Meshed model of the specimen and the loading/support balls, Model 3.

2.1.2. Simplified model for square plates

Model 2 serves the same purpose as Model 1A, but for square plates. Due to the reduced symmetry of the system, one half of the plate has to be simulated, as displayed in Fig. 3. Both the loading and the support balls were represented by a punctiform load (or boundary condition) applied in the center of the disc and at the support radius R_s, respectively. The specimen was meshed with a minimum of 162216 SOLID95 elements and 682140 nodes, depending on the specimen's thickness and overhang.

2.1.3. Complete 3D-Model for discs

Model 3 serves as a validation for the simplified models. It represents a 3D-model of the testing assembly, based on a model first developed by Börger et al. [30]. Symmetry conditions allowed a reduction to one sixth of the full testing assembly, see Fig. 4. The specimen was meshed with a minimum of 40392 SOLID95 elements and 173061 nodes and a maximum of 70668 SOLID95 elements and 301375 nodes, depending on the specimen's thickness and overhang. The loading ball was meshed with 1750 SOLID95 elements and 8196 nodes, the support ball using 3500 SOLID95 elements and 15582 nodes. The contact between the loading ball and the specimen was meshed with 375 CONTA174 (8-node surface elements) and 375 TARGET170 elements (8-node surface elements), the contact between the support ball and the specimen with 490 CONTA174 and 490 TARGET170 elements. The friction coefficient was set to $\mu = 0.5$ and symmetric contact calculations were employed. Since this model includes interactions between the specimen and the balls as well as load-dependent changes to the testing assembly and is solved under non-linear conditions, a better representation of real testing situations is given. A mesh convergence analysis for this and the other mentioned models can be found in Appendix A of this work.

2.2. Analytic solution for the deflection of plates

Kirstein et al. already developed an analytical solution for the deflection of thin centrally loaded plates on symmetric point supports in 1966 [33]. This solution is valid for a minimum of three supporting points up to a theoretical maximum of an infinite number of support points, which would represent a ring supported situation. Within the context of this paper, their solution will be utilized for the special case of $m = 3$ support points and a central punctiform load. The deflection w at a position with radial distance r from the center of a disc with radius R and supported on points with distance D_s from the evaluated position is given by:

$$w = w_0 + \frac{3P(1-v^2)}{2\pi Et^3}\left(r^2\ln\rho - \frac{1}{m}\sum_{s=1}^{m}D_s^2\ln\frac{D_s}{c}\right) \tag{1}$$

with

$$w_0 = \frac{P(1-v^2)}{2\pi\kappa Et^3}\left[\sum_{s=1}^{m}D_s^2\ln\frac{D_s'}{r_s'} + \left(\kappa^2 - 1\right)c^2 Re\{L_m(\zeta)\} + \frac{m(1-\rho^2)R_s^2}{\kappa+1}\right] + \gamma_3 \tag{2}$$

and

$$\gamma_3 = \frac{3P(1-v^2)R_s^2}{2\pi\kappa Et^3}\left[A_m(\beta) + \left(1-\kappa^2\right)B_m(\beta) - \kappa\ln\beta - \frac{1-\beta^2}{\kappa+1}\right]. \tag{3}$$

Here, P denotes the applied load, E the specimen's Young's modulus, t the specimen's thickness, R_s the support radius, β the ratio R_s/R, and v the Poisson's ratio of the specimen. Other parameters of the equation will not be discussed here, the authors refer to the original work by Kirstein et al. [33].

2.3. Fitting

Every fit in this work has been performed in Mathematica 13.1 (Wolfram Research, IL 61820, Champaign, USA) with the command *NonlinearModelFit*. This command performs a least sum of squared errors fit on any given type of ansatz function by adjusting user-specified constants within the function. The deviation between the value of the fit $x_{i,fit}$ and the fitted data $x_{i,ref}$ for data point i will be referred to as residual error and is determined by

$$Residual \quad error \quad [\%] = 100.\frac{x_{i,fit} - x_{i,ref}}{x_{i,ref}} \tag{4}$$

For each fit, the maximum positive and negative residual error for the complete data field will be given. Furthermore, the mean residual error for a fit based on n grid points is given by

$$Mean \quad residual \quad error \quad [\%] = 100.\frac{\sum_{i=1}^{n}\text{Abs}\left(\frac{x_{i,fit} - x_{i,ref}}{x_{i,ref}}\right)}{n}. \tag{5}$$

3. Simplifying the stress calculation

3.1. Discs

Due to the lack of an accurate analytical solution for the stress field, it must be numerically evaluated instead. Börger et al. [30] performed Finite-Element-analysis for the special case of contacting support balls. If not stated otherwise, this assumption will be maintained throughout this work. For this case, the support radius R_s is given by the radius of the support balls R_{SB} by

$$R_s = R_{SB}\frac{2}{\sqrt{3}}. \tag{6}$$

In general, the maximum tensile stress σ_{max} in the center of a bent plate scales with the applied load P and the inverse square of the thickness of the plate t:

$$\sigma_{max} = f\frac{P}{t^2} \tag{7}$$

The factor f is a dimensionless function which takes the material

Table 1

Constants m_1-m_3 utilized in Eq. (9).

m_1	m_2	m_3
0.697	-0.118	-0.728

Table 2

Accuracy parameters describing the deviation of Eq. (9) to the data field for discs and Eq. (10) used in Eq. (9) to the data field for square plates.

Accuracy parameter	Discs	Square plates
Maximum residual error [%]	+ 1.4	+ 1.6
Minimum residual error [%]	-1.9	-1.6
Mean residual error [%]	+ 0.52	+ 0.63

properties and the involved geometry into account. Within their work, they reduced the factor f for the B3B-test to being dependent on the specimen's thickness t, the specimen's radius R, the support radius R_s and the Poisson's ratio v. Furthermore, the results of a parametric study were made available by providing a fitted function for f:

$$f_{B\ddot{o}rger}\left(\frac{t}{R},\frac{R_s}{R},v\right) = c_0 + \frac{c_1 + c_2\frac{t}{R} + c_3\left(\frac{t}{R}\right)^2 + c_4\left(\frac{t}{R}\right)^3}{1 + c_5\frac{t}{R}}\left(1 + c_6\frac{R_s}{R}\right) \quad (8)$$

This function covers the range of $0.55 \leq R_s/R \leq 0.9$, $0.05 \leq t/R \leq 0.6$ and $0.2 \leq v \leq 0.3$. This range was later extended to $0.1 \leq v \leq 0.4$ by Danzer et al. [32]. The value of $f_{B\ddot{o}rger}$ determined with this fit has an error $\leq \pm 1\%$ with respect to the numerical solution. This accuracy is made possible by providing a set of constants c_0-c_6 for different Poisson's ratios in an increment of 0.05; a total of 49 constants. If the tested material has a Poisson's ratio not tabulated, linear interpolation must be performed. This makes implementation of this equation prone to errors and cumbersome. In order to simplify the calculation of the maximum stress, a new study on f has now been conducted. Up to now, f was always expressed and evaluated with its arguments relative to R. However, the influence of the support radius R_s on the value of f is significantly higher than that of the specimen's radius R. Therefore, a new data field for f based on the now modified parameters t/R_s, R/R_s and v was generated by FEA utilizing Model 1, with a total of 1400 datapoints. The data field covers $1.05 \leq R/R_s \leq 2$, $0.05 \leq t/R_s \leq 0.6$ and $0.1 \leq v \leq 0.4$. Based on this data, a new empirical fit was developed. Now, the factor f can be determined by

$$f_{new}\left(\frac{t}{R_s},\frac{R}{R_s},v\right) = \exp\left[m_1(1+v) + m_2 ln\frac{t}{R_s} + m_3\sqrt[4]{\frac{Rt^2}{R_s^3}}\right] \quad (9)$$

with m_1-m_3 as listed in Table 1 and the limits of valid application as the range of the fitted data field.

An overview of the general deviation from Eq. (9) to the fitted data can be found in Table 2. Fig. 5a)-e) provide a more comprehensive overview of the fit's accuracy. In terms of specimen geometry, the lowest accuracy/largest deviation is generally found in the peripheral regions. Similarly, a low accuracy for exceptionally low and high Poisson's ratios can be observed. However, most technical ceramics exhibit a Poisson's ratio in the range of 0.2 – 0.3 [31], a range well described by the fit. Furthermore, typical specimens for the Ball-on-Three-Balls-test exhibit geometries as marked in Fig. 5c). Here, a maximum and minimum deviation as low as + 0.15% and − 0.7%, respectively, are achieved. In principle, a small loss in (overall) accuracy as compared to the fit by Börger et al. [30] is observed, though only in regions of minimal interest. Fig. 5 further gives the possibility to derive highly accurate strength results for individual geometries by utilizing the given deviation in combination with Eq. (9) to determine the applied stress as originally calculated with FEA.

3.2. Square plates

Another very common specimen geometry are square plates, which can be tested in similar testing fixtures as discs. The factor f for these specimens does not deviate much from similarly sized disc-shaped specimens, but the difference is large enough to necessitate a separate treatment. This is due to the fact that the overhang, i.e. the part of the specimen from the outer edge to the support radius, has a small but still pronounced effect on the maximum tensile stress. Therefore, instead of describing square plates with fit very similar to Eq. (9), the authors opted to provide a conversion from square plates to equivalent discs, as has been done for other methods [4,34]. An equivalent disc is defined by its diameter D_{eff}, which is chosen in a way so that the maximum stress is the same as in the square plate specimen. All other geometry parameters, such as the specimen's thickness and the support radius, remain unchanged. Therefore, only the conversion from the square plate's edge length L to the equivalent diameter is needed. In order to derive this conversion, Model 2 was utilized and 1035 datapoints were generated. The data field covers $2.165 \leq L/R_s \leq 3.899$, $0.0449 \leq t/R_s \leq 0.736$ and $0.05 \leq v \leq 0.45$. Based on this data, a conversion from square plates to discs was developed. The effective diameter D_{eff} is determined by

$$D_{eff} = L\left(1.053 - 0.017\frac{tL}{R_s^2}\right). \quad (10)$$

An overview of the deviation for the factor f, derived with the conversion to equivalent discs and Eq. (9), to the FEA-data for square plates can be found in Table 2.

It should be noted that this conversion is only valid in the range $2.17 \leq L/R_s \leq 3.9$, $0.1 \leq t/R_s \leq 0.6$ and $0.1 \leq v \leq 0.4$.

4. Improving accuracy for high-load testing situations

So far, all simulations have been conducted with Models 1A and 2 described in Sections 2.1.1 and 2.1.2. As previously stated, this model represents the ideal case during testing with both punctiform load introduction and support conditions. It is evident that this will not represent reality in a number of practical cases and that some errors are to be expected. Errors due to geometric deviations of various aspects of the testing setup have already been discussed by Börger et al. and deemed negligible [25]. Therefore, the aforementioned errors mostly arise because no interactions between the loading or support balls and the specimen are represented in the model. First, an increase in load results in deformation of the loading ball and the specimen in the area of contact, whereby the assumption of punctiform load introduction loses its validity. Instead, a finite area of contact and load introduction is established. Second, large deflection of the specimen may occur under certain conditions, causing it to roll off the support balls. This results in a shift of contact position towards the center of the support circle, altering the applied bending moment and with it the maximum tensile stress. Third, friction between the loading ball and the specimen can have a significant influence on the maximum tensile stress of the specimen. It induces shear stresses under the area of contact, which act through the specimen thickness and thus reduce the maximum tensile stress.

Due to these interactions being included, Model 3, as described in Section 2.1.3, is significantly better suited to provide an accurate representation of reality. This then provokes the idea of using this model in a similar way to the previous section and incorporate all the mentioned effects into the evaluation at once. The main drawback of this model is its high processing time due to its use of contact calculations despite a decrease in the overall number of elements. In general, the evaluation takes about 70–80 times longer than for Model 1A. In order to represent the mentioned effects in the calculation of maximum stress, a higher number of parameters would be needed. First, the load-dependence has to be considered, which is influenced by the elastic constants of both the specimen and the support or loading balls. This would result in the
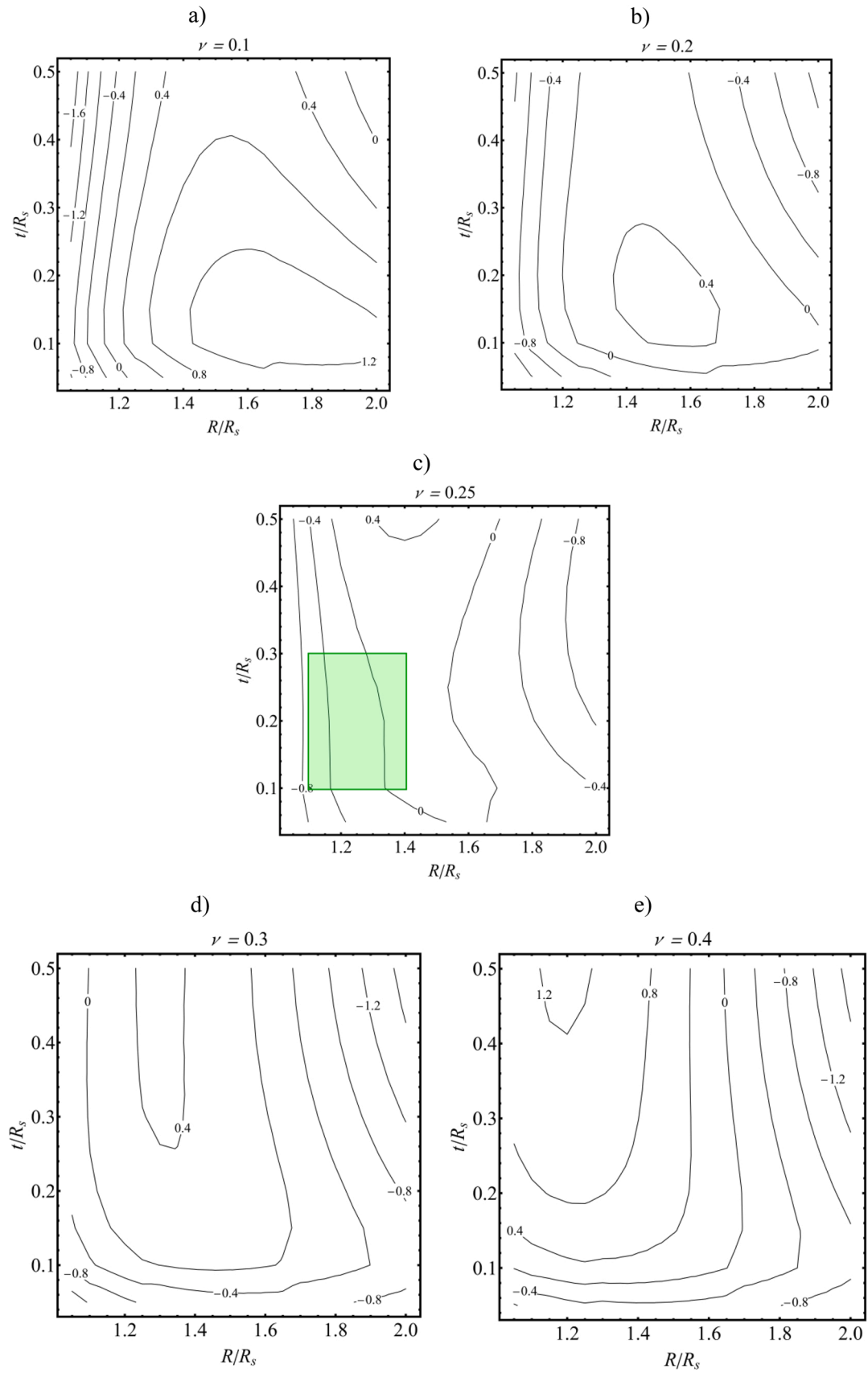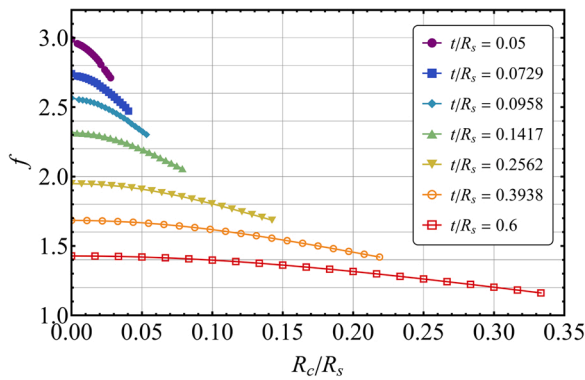
a)

$\nu = 0.1$

b)

$\nu = 0.2$

c)

$\nu = 0.25$

d)

$\nu = 0.3$

e)

$\nu = 0.4$

Fig. 5. Overview of the relative error of f_{new} to the fitted data points.

Fig. 6. The factor *f* in dependence of the relative contact radius and the specimen's relative thickness as predicted by FEA. Values at $R_c/R_s = 0$ are those which correspond to the point-load situation, and which are described by Eq. (7).

Table 3
Constants h_1-h_5 utilized in Eq. (12).

h_1	h_2	h_3	h_4	h_5
1.0052	0.00063	-0.5928	1.6756	1.3523

Table 4
Accuracy parameters describing the deviation of Eq. (12) and Eq. (15) to their respective fitted data fields.

Accuracy parameter	k_1	s_{red} (k_2)
Maximum residual error [%]	+ 1.0	+ 6.4
Minimum residual error [%]	-0.50	-13
Mean residual error [%]	0.16	3.7

addition of up to four new parameters. To properly capture each dependency, each relevant parameter would have to be varied within its relevant range in at least 10 steps. Putting all those considerations together, a new parameter field with a size well within millions of data points would be necessary. In combination with the high processing time, a study like this would require immense computing power. Developing an accurate fit for such a data field would be another challenge by itself.

Therefore, a different method has to be considered. Within this work, a separation approach will be utilized. By taking an individual look at each major effect, a better understanding of its consequences can be achieved. Ideally, the deviations from the ideal solution f_{new} caused by them can be described separately with correction factors k_i. Combining these expressions multiplicatively, as shown in Eq. (11), will yield a corrected factor f_{corr}. If each k_i is a somewhat manageable functional expression with sufficiently similar results to FEA, this method will provide a valuable alternative evaluation, but within a much shorter time.

$$f_{corr} = f_{new} \prod_i k_i \qquad (11)$$

In the upcoming sections, a closer look at the change in load application and the specimen's deflection will be taken and functional expressions to describe their influence on the factor *f* will be provided.

4.1. Contact at the loading ball

As mentioned in the previous section, an increase in load establishes a finite area of contact between the loading ball and the specimen. This causes a change in load introduction from the ideal punctiform load to a distributed load over a circular contact area at the center of the specimen. The size of this area will be quantified by its radius, which will be referred to as the contact radius R_c. In principle, an increase in contact radius reduces the bending moment and with it the stress applied on the specimen. This change in stress has been investigated by FEA with Model 1B described in Section 2.1.1. Instead of a punctiform load, a Hertzian pressure distribution for the contact between a sphere and a flat surface has been applied. With this model, a parametric study of approximately 6000 simulations on the influence of the contact radius R_c on the maximum stress (i.e. the factor *f*) has been conducted. More specifically, the contact radius R_c was varied for a wide range of specimen geometries, such as the specimen's thickness *t*, the specimen's radius *R* and the support radius R_s. Additionally, the influence of the applied load *P*, the specimen's Young's modulus *E* and Poisson's ration *v* was investigated as well. In conclusion, only the contact radius, specimen's thickness and support radius have a distinct influence on the maximum stress. The other parameters mentioned have an influence on the contact radius, but

not on the maximum stress directly. This allowed to reduce the number of relevant parameters to just three. By using dimensionless relative parameters, e.g. the relative contact radius R_c/R_s and relative thickness t/R_s, the number of parameters could be further reduced to two. Based on these findings, a reduced data field with 525 data points to describe the change in maximum stress, i.e. the factor *f*, was generated. The influence of these two parameters on *f* is shown in Fig. 6.

By fitting this data field, a functional expression for the change of *f* due to the change in contact area can be provided. The correction k_1 can be given as

$$k_1(a/R_s, t/R_s, v, E, E_{LB}, v_{LB}, P) = h_1 + h_2 \ln(R_c/R_s \cdot t/R_s) + h_3 \frac{(R_c/R_s)^{h_4}}{(t/R_s)^{h_5}} \qquad (12)$$

where

$$R_c = \sqrt[3]{\frac{3PR_{LB}}{4}\left(\frac{1-v^2}{E} + \frac{1-v_{LB}^2}{E_{LB}}\right)} \qquad (13)$$

with R_c describing the contact radius based on the Hertzian solution. E_{LB} and v_{LB} are the Youngs's modulus and Poisson's ratio of the loading ball, respectively. R_{LB} denotes the radius of the loading ball. The fitting constants h_1-h_5 are listed in Table 3. An overview of the deviation of Eq. (12) to the fitted data can be found in Table 4.

4.2. Deflection of the specimen

A different problem is raised through the interaction of the specimen and the support balls. With increasing specimen deflection, the point of contact progressively shifts inwards. This reduces the applied bending moment due to decreasing leverage. Since the bending moment is directly proportional to the maximum stress and therefore the factor *f*, a functional expression for the change in bending moment is equal to the searched correction k_2. This effect is especially pronounced when materials with high strength (> 1000 MPa) and low Young's modulus (< 100 GPa), such as high-strength glass, are tested. In order to predict the extent of this effect, the change in leverage, i.e. the shift in contact position at the support balls, has to be known. By considering the geometry of the problem, trigonometry can be utilized to express the shift in contact x_{shift} from the slope s_{con} of the specimen with

$$x_{shift} = R_{SB} \sin \arctan s_{con}, \qquad (14)$$

where R_{SB} is the radius of the support ball. A schematic of the geometric relations is shown in Fig. 7.

Therefore, the problem can be reduced to the determination of the slope of the specimen's deflection curve at the point of contact. Ideally, this information can be directly deduced from an analytical expression. Favorably, Kirstein et al. [33] derived an analytical description for the deflection of point-loaded plates on an arbitrary number of equally spaced point supports, as explained in Section 2.2. If we differentiate a
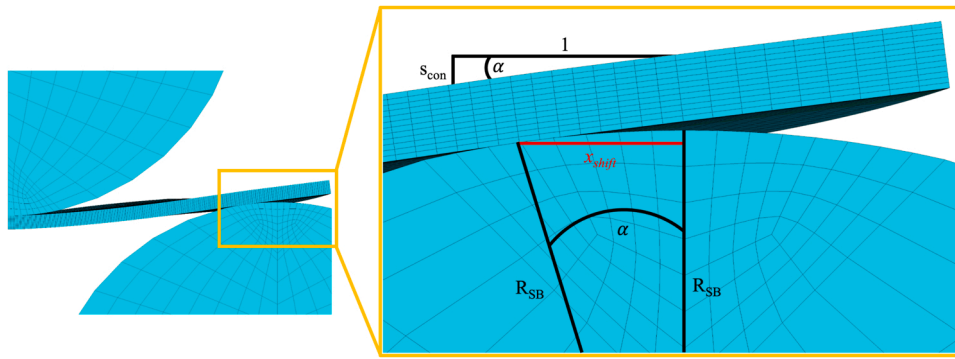
Fig. 7. Geometric relations for the contact point shift between the specimen and the support ball.

function describing the deflection of a specimen, a function describing its slope is obtained. However, due to its complexity, this cannot be done analytically for the solution by Kirstein et al. Therefore, a numerical approach had to be employed. First, the number of variables for the numerical evaluation had to be reduced. This was done by factoring out P/Et^2, which leaves a reduced function for the deflection that is independent of the applied load and the specimen's Young's modulus. Therefore, the variables had been narrowed down to R, R_s, v and t. By forming dimensionless relative parameters, i.e. the relative radius R/R_s and relative thickness t/R_s, the number of parameters could be further reduced to three. A parametric study on those three parameters for the reduced slope at the point of support was conducted and a data field comprising 1330 data points was generated. By fitting, an approximation for the analytical derivation of the equation by Kirstein et al. at this position can be given. The fit for the reduced slope s_{red} can therefore be expressed as

$$s_{red} = \left(1 - v^2\right)\frac{R/R_s}{t/R_s}\left(0.0015 - 1.13\frac{1}{\left(R/R_s\right)^2}\right). \tag{15}$$

A summary of the deviation of Eq. (15) to the fitted data can be found in Table 4. The high relative deviation stems from the deviation for low absolute values of the reduced slope. Here, a small deviation in absolute value causes a large relative deviation due to the reference value being very small. This large error would therefore only come into play when very small deflections are involved, a case where an application of this fit or correction is neither necessary nor recommended. Combining the reduced slope with the load- and material-specific term previously factored out yields the actual slope s_{con} at the contact point between the specimen and the support ball

$$s_{con} = \frac{P}{Et^2}\left[\left(1 - v^2\right)\frac{R/R_s}{t/R_s}\left(0.0015 - 1.13\frac{1}{\left(R/R_s\right)^2}\right)\right] \tag{16}$$

with the variables as denoted in previous equations. Since the slope at the point of contact is now known, Eq. (14) can be utilized to predict the shift in contact position x_{shift} with

$$x_{shift} = R_{SB}\sin\arctan\frac{P}{Et^2}\left[\left(1 - v^2\right)\frac{R/R_s}{t/R_s}\left(0.0015 - 1.13\frac{1}{\left(R/R_s\right)^2}\right)\right] \tag{17}$$

Due to the small value of the argument of the trigonometric functions, s_{con}, a small angle approximation ($\sin\arctan x \approx x$) can be performed. This then gives

$$x_{shift} = R_{SB}\frac{P}{Et^2}\left[\left(1 - v^2\right)\frac{R/R_s}{t/R_s}\left(0.0015 - 1.13\frac{1}{\left(R/R_s\right)^2}\right)\right] \tag{18}$$

for x_{shift}. In order to predict the change in bending moment, the relative change in leverage has to be calculated. This is done by subtracting x_{shift} from the original lever arm, i.e. the support radius R_s, and then dividing

the result by R_s. Since the slope determined with Eq. (16) is negative, x_{shift} is negative as well and has to be added to R_s instead in order to correctly portray the change in leverage. This then yields

$$k_2 = \frac{R_s + x_{shift}}{R_s} \tag{19}$$

for the change in bending moment k_2. Inserting Eq. (17) into Eq. (19), utilizing the relationship from Eq. (6) and simplifying the resulting expression gives

$$k_2 = 1 + \frac{\sqrt{3}}{2}\frac{P}{Et^2}\left[\left(1 - v^2\right)\frac{R/R_s}{t/R_s}\left(0.0015 - 1.13\frac{1}{\left(R/R_s\right)^2}\right)\right] \tag{20}$$

4.3. Friction & plastic deformation of the loading ball

The influence of friction and plastic deformation has been investigated through FEA with a model employing contact calculations. It was found that friction between the specimen and the loading ball starts to play an increasingly important role if the specimens are thin. For thin and highly flexible specimens, i.e. $t/R_s = 0.05$ and $E = 70$ GPa, a reduction in the maximum tensile stress of about 4% from the frictionless case to the same setup with $\mu = 0.5$ has been observed. This is due to the shear stresses caused by friction starting to affect the stress at the opposing face, resulting in a reduction of maximum tensile stress. For thicker and less flexible specimens, this effect is in the range of about 1–2%. As will be explained in the upcoming sections, thin and flexible specimens are difficult to describe with the models established in this work and will have to be treated separately. Since this effect is only significant for a small portion of possible specimen geometries, while having only a minor influence on the remaining ones, no functional expression for the influence of friction will be provided. Additionally, friction between the support balls and the specimen is not present if the balls are allowed to rotate freely [25].

Another possible source of error is plastic deformation of the loading ball. The expected effect would be similar to what has been covered in Section 4.1. A FE study using an ideal bilinear elastic-plastic material model for the loading ball [35], solely for the influence of plastic deformation on the contact situation, was conducted. It revealed a nearly linear relation between the increase in load and the increase in contact radius compared to the pure elastic case. If the material properties of the balls are known, this additional increase can be determined and added to the elastic deformation. This would provide a new contact radius R_c' for the usage in k_1 and no further changes to the calculation of the maximum tensile stress would have to be made.

4.4. The load-corrected stress evaluation

Combining the correction factors k_1 and k_2 with f_{new} ultimately yields the corrected factor f_{corr}

Table 5
Material parameters for "typical" specimens.

Specimen material	R/R_s [-]	E [GPa]	v [-]
Glass	1.2	70	0.22
Zirconia		210	0.25
Alumina		420	0.2

$$f_{corr}\left(\frac{t}{R_s}, \frac{R}{R_s}, v, E, v_{LB}, E_{LB}, P\right) = f_{new}k_1k_2 \tag{21}$$

which now takes additional load- and material-dependent effects into account. The following sections will provide an overview of the performance and accuracy of this functional expression for f_{corr}.

5. Validation and Comparison of f_{corr}

Before the comparison of f_{corr} to FEA results obtained with Model 3, some aspects of the behavior of the correction factors k_1 and k_2 have to be discussed. First, thin specimens exhibit the highest relative deflections and with it the strongest curvature. This especially affects the size of the zone of contact between the loading ball and the specimen, where the curvature is most pronounced. As discussed in Section 4.1, the size of the contact area has a strong effect on the maximum stress. However, the correction factor k_1 is based on the assumption of Hertzian contact between a sphere and a flat surface. This suggests a smaller area of contact compared to contact between a sphere and a concave surface. Therefore, k_1 underestimates the effect of contact for large deflections. Second, the geometric assumptions necessary for the equation given by Kirstein et al. [33] lose their validity for large deflections. Due to the correction factor k_2 being deducted from this equation, an error for

exceptionally thin specimens is expected. A comparison of the slope at the point of contact as obtained with FEA and the prediction by Eq. (1) for thin specimens with large deflections shows an overestimation by the analytical solution. Additionally, Kirstein et al. assume punctiform load introduction, while an extended load introduction is closer to real testing situations. This reduces the applied bending moment and with it the deflection, which is another reason for the overestimation of the slope at the point of contact. Therefore, the correction factor k_2 generally overestimates the effect of deflection for exceptionally thin specimens.

Model 3 mentioned in Section 2.1.3 was utilized as a base of comparison and a tool for the validation of Eq. (21). More specifically, the load dependency of the factor f was determined with both methods for a range of parameters. On one hand, this range includes "typical" specimens and testing setups, as one would encounter on a regular basis. On the other hand, the edge-cases of possible parameter combinations were also examined to work out the limits of Eq. (21)'s applicability. All comparisons in this chapter are based on a testing setup that utilizes steel balls with a Young's Modulus of 210 GPa and a Poisson's ratio of 0.33. For typical specimens, a relative radius R/R_s of 1.2 and a range of relative thicknesses t/R_s from 0.05 to 0.4 were chosen. The material-specific parameters are listed in Table 5. Fig. 8a)-c) depict the change in f in dependence of the applied load P, predicted by both FEA and Eq. (21). The corresponding maximum stress for each curve is approximately 2 GPa. Except for specimens with a relative thickness of 0.05, exceptional agreement between the two methods is achieved. The maximum relative error for specimens with $t/R_s \geq 0.1$ is less than 1%. It should be noted that FEA was conducted with non-linear geometric behavior considered, which is represented accurately by the functional expressions.

Eight edge-cases were investigated to cover extreme specimen

a)

b)

c)
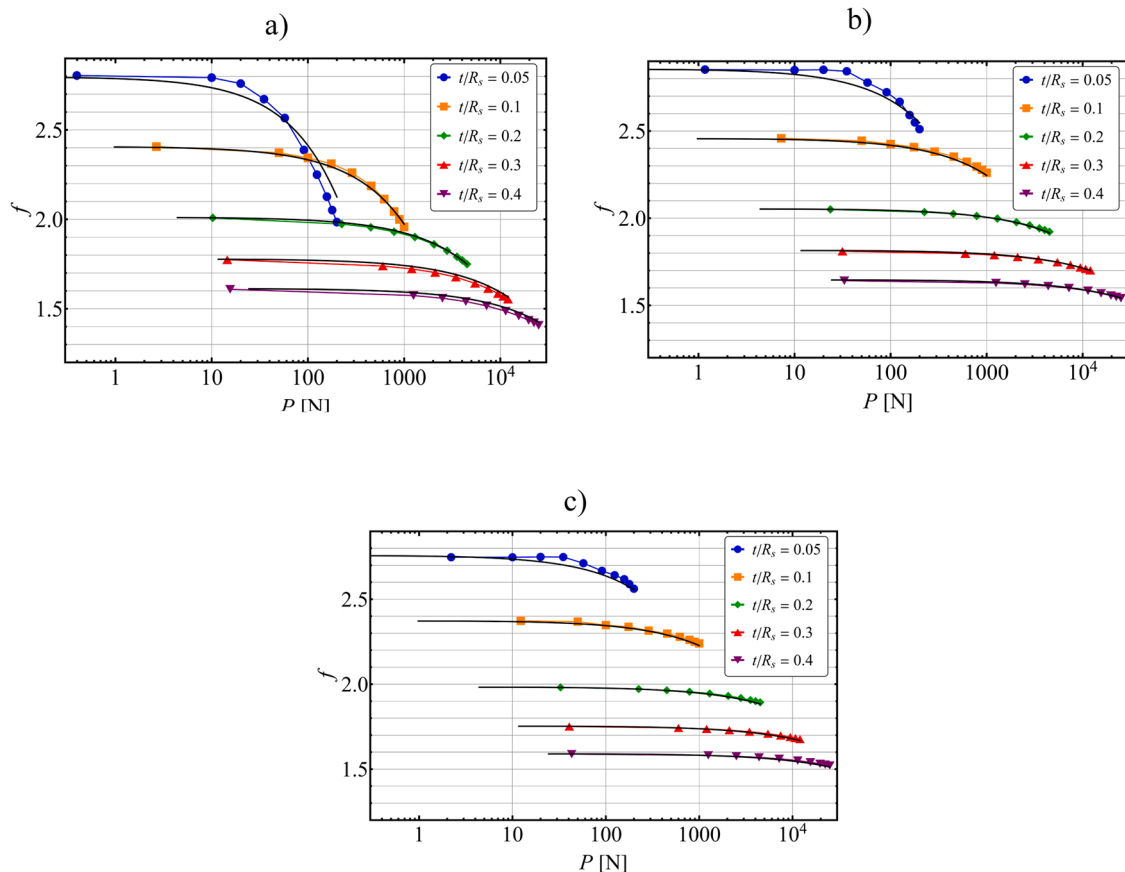
Fig. 8. Dependence of f on the applied load P as predicted by FEA and by Eq. (21). The colored markers represent the results of FEA, the continuous black line represents f_{corr}, Eq. (21). The maximum tensile stress for each curve is approximately 2 GPa. The results for glass are shown in a), zirconia in b) and alumina in c).

Table 6

Geometry and material parameters as well as the maximum relative deviation from f_{corr} to FEA for a number of investigated edge cases.

Designation	R/R_s [-]	E [GPa]	v [-]	Max. dev.
Case 1	1.05	70	0.1	< 2%
Case 2			0.4	< 2%
Case 3		420	0.1	2%
Case 4			0.4	< 2%
Case 5	1.525	70	0.1	6%
Case 6			0.4	< 2%
Case 7		420	0.1	< 2%
Case 8			0.4	< 2%

Table 7

Parameter range for the accurate application of Eq. (21).

t/R_s [-]	R/R_s [-]	E [GPa]	v [-]	σ_{max} [MPa]
0.1 – 0.5	1.05 – 1.525	70–420	0.1 – 0.4	≤ 2000

Note that for the special case of specimens similar to case 5, i.e. highly flexible specimens ($E \leq 100$ GPa) with a high strength ($\sigma_F \geq 1$ GPa) and a Poisson's ratio in the range of 0.1–0.15, deviations of up to 6% are expected.

geometries and extreme material properties. As before, the relative thickness was varied, but now in the range from 0.05 to 0.5. Two main cases were differentiated: An exceptionally small relative radius of 1.05 (i.e. a small overhang) and large relative radius of 1.525 (i.e. large overhang). Within each case, 4 combinations of material parameters were evaluated. The specific parameters are listed in Table 6. Fig. 1 of the supplementary material depicts the results for cases 1–4, while Fig. 2 of the supplementary material depicts the results for cases 5–8. Again, specimens with a relative thickness of 0.05 exhibit the highest deviation, with the exception of case 2 and 8, and will not be included in the following observations. For cases 1–4, i.e. specimens with very low relative radius, an overall good agreement is observed. The highest deviation is displayed in case 3 by the specimen with a relative thickness of 0.1. However, the maximum deviation for this specific combination of parameters is about 2%, which is well within the desired accuracy. For cases 5–8, i.e. specimens with a very high relative radius, a similar situation is found. Cases 6–8 exhibit good agreement, only the specimen with a relative thickness of 0.1 in case 7 displays a deviation of about 1.6%. Case 5 however indicates a problem for highly flexible specimens with a low Poisson's ratio. Here, even the thickest specimen exhibits a constant deviation of about 4%. The specimen with a relative thickness of 0.1 exhibits an error of up to 5.9%, albeit only for a maximum stress of more than 1 GPa.

As discussed in the beginning of this chapter, both corrections either underestimate (k_1) or overestimate (k_2) their respective influences with increasing load. Due to the factors k_1 and k_2 being utilized in multiplicative combination, these errors cancel each other out and an accurate description can evidently be achieved for most specimens. However, they cannot sufficiently describe specimens with a relative thickness < 0.01. Considering these aspects, the range of parameters for the application for f_{corr}, i.e. Eq. (21), is given in Table 7. Since f_{corr} has been compared to FEA only up to a maximum tensile stress of 2 GPa, the authors do not recommend application for specimens with a higher strength. Within the given range, Eq. (21) replaces individual FEA with an error typically ≤ ± 2%.

6. Practical aspects

The test set-up of the B3B-test was originally designed using three contacting balls to provide the support of the specimen on a perfect circle and a ball of similar size as loading ball, as depicted in [25,30]. Due to the ability of the support balls to rotate at their position during

Table 8

Summary of the valid parameter ranges for the functional expressions of f.

|	t/R_s	R/R_s or L/R_s	E [GPa]	v	σ_{max} [MPa]
f_{new}	0.1 – 0.6	1.05 – 2	–	0.1 – 0.4	material specific, Eq. 23
$f_{new, square}$	0.1–0.6	2.17 - 3.9	–	0.1 – 0.4	material specific, Eq. 23
f_{corr}	0.1 – 0.5	1.05– 1.525	70–420	0.1 – 0.4	≤ 2000
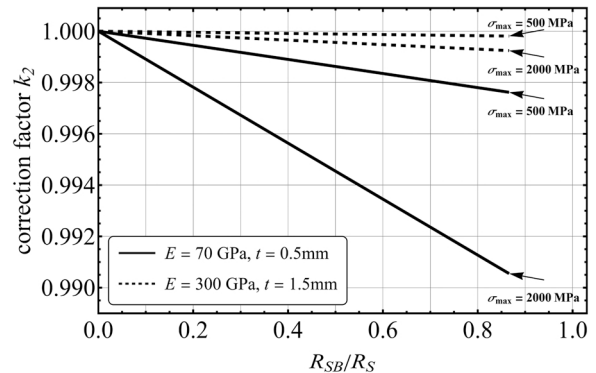
Fig. 9. Correction factor k_2 for exemplary specimens ($R = 6$ mm, $R_S = 5$ mm) in dependence of the radius of the support balls (in fractions of the support radius). Through lines represent thin, flexible (glass) specimens ($t = 0.5$ mm, $E = 70$ GPa), dashed lines represent thicker, more typical ceramic specimens ($t = 1.5$ mm, $E = 300$ GPa). Two cases are shown: $\sigma_{max} = 500$ MPa and $\sigma_{max} = 2000$ MPa.

the test, friction can be minimized, and an important source of error can be eliminated [25]. Furthermore, this set-up facilitates jig-designs with exceptionally easy handling. Preferably, ball bearing grade steel balls are used, since they are easy to obtain and available in a fine grading of radii over a wide range of sizes. The separate description of the influences of two important issues of the B3B test – the contact situation through k_1 and the deflection effects through k_2 - paves the way to an analysis of some practical aspects of the test. In the following sections, these aspects will be discussed within the validity range of Eq. (21), as given in Table 8, for exemplary specimens with radius of $R = 6$ mm on a support radius of $R_s = 5$ mm. The ideal ball radius for this set-up is $R_{SBi} = R_{LBi} = 4.33$ mm.

6.1. Support ball size

In Section 4.2 and in Eqs. (17) and (19), the influence of the specimen's deflection on the maximum stress in the specimen is described and quantified. It is obvious that this effect is more pronounced if the specimen is supported on large balls. The influence of the shift of contact on the maximum stress can be reduced if smaller than ideal support balls are used. For any test geometry, the correction factor k_2 depends linearly on the ratio of the support ball radius over support radius, R_{SB}/R_S. For $R_{SB}/R_S = 0$, $k_2 = 1$, for larger ratios $k_2 < 1$. This trend is illustrated in Fig. 9 for thin specimens with a Young's modulus of $E = 70$ GPa and more typical, thicker specimens with $E = 300$ GPa at two failure stresses. It can be seen that the effect of using smaller support balls is very small unless very flexible materials with extremely high strength are tested. Using smaller balls will also require a new design of the test fixture, which will certainly be more complicated than the one suggested earlier [25,30], especially regarding the exact positioning of the support balls and their ability to rotate.
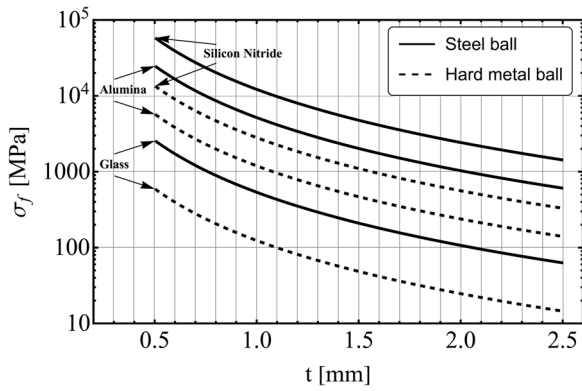
Fig. 10. Strength-thickness map for B3B-tests on exemplary specimens ($R = 6$ mm, $R_S = 5$ mm) of glass, alumina, and silicon nitride. If the measured strength of a specimen with a given thickness t is below its respective line, no contact cracks are expected. The through lines refer to loading with a steel loading ball with the ideal radius $R_{LBi} = 4.33$ mm, the dashed lines refer to loading with hard-metal ball with $R_{LB} = 1$ mm.

6.2. Contact of the specimen with the loading ball

The ideal loading situation in the B3B-test is a punctiform load introduction. Of course, this cannot be achieved using a ball to apply the load. It has been shown in Section 4.1 how an increase in the size of the area of load introduction influences the maximum stress. In practice, the desirable situation of keeping the size of this area as small as possible is favored by two means: by using a loading ball with a higher Young's modulus (see Eq. (13) or by using a smaller loading ball (i.e. smaller than the ideal size which is equal to the contacting support balls). Eqs. (12) and (13) can be employed to evaluate the influence of using a hard metal loading ball of ideal size with a Young's modulus of $E_{LB} = 600$ GPa instead of steel balls. This only has a negligible influence of less than 1% on the correction factor k_1. The effect of using a smaller loading ball is slightly more pronounced, with deviations up to 3% for very small balls. These numbers were obtained for the condition of a maximum tensile stress of 2000 MPa in the specimens. The effect will be even smaller at lower stresses.

Moreover, any contact of a ball with a surface, as at the site of load introduction in the B3B-test, bears the risk of the formation of contact cracks if a certain critical load P_c is exceeded [36]. Upon increase of the load beyond this critical value such cracks may grow, penetrate the thickness of the specimens and lead to failure [37]. This is an unwanted situation that can be avoided if the load at fracture due to bending, P_f, is less than the critical load P_c for the formation of contact cracks, i.e. $P_f < P_c$.

For common ball sizes used in the B3B test, this situation can be analyzed by using Auerbach's law for the contact between a flat surface and a ball. According to Auerbach's observations [38], the load required to produce contact cracks P_c is proportional to the radius of the loading ball: $P_C = A \cdot R_{LB}$. The constant A (Auerbach constant) has been related to the elastic constants of the involved materials and the surface energy γ of the cracked material [39,40], and has further been determined experimentally for various material (i.e. specimen and ball) combinations [41–45]:

$$P_c = \frac{3\pi^3}{16} \frac{1}{\phi_a} \left(\frac{1-\nu^2}{E} + \frac{1-\nu_{LB}^2}{E_{LB}} \right) \frac{2\gamma}{(1-\nu^2)} \frac{E}{R_{LB}} \tag{22}$$

Eq. (22) or experimental values for A can be used to plot curves of $\sigma(P_c)$, using Eq. (7), for a given specimen geometry as a function of the specimen's thickness t. Such curves can be used to find limiting conditions for contact cracking during B3B-tests. An example for such curves for the exemplary specimen is given in Fig. 10 for various specimen materials (glass, alumina, silicon nitride) and a steel loading ball of ideal
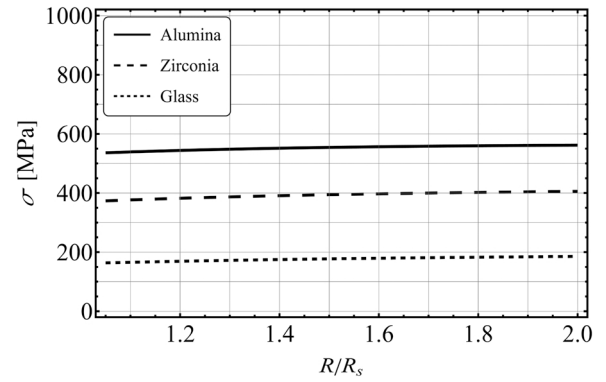
Fig. 11. 2%-Limit for selected specimens with varying Young's modulus in dependence of R/R_s.

size R_{LBi}. If the expected strength of the specimen is below the line at a given thickness, no contact cracks should be generated during the B3B-test. For glass, $A = 62$ N/mm was taken from [41], for alumina, $A = 590$ N/mm from [42] and for silicon nitride, a value of $A = 1360$ N/mm using materials properties given in [46], Eq. (22) $\phi_a = 0.0011$ [39] and the relation $K_{Ic}^2 = 2\gamma E/(1-\nu^2)$ was used. Additionally, Fig. 10 depicts the same limit curves for a loading ball made from hard-metal and with a radius $R_{LB} = 1$ mm.

It is obvious from Eq. (22) how the size and Young's modulus of the loading ball influence the limit curve: the smaller R_{LB}, the smaller is P_c and the higher E_{LB}, the smaller is A. Both trends shift the limit curve towards lower strength values. These findings discourage the use of smaller or stiffer loading balls. However, the use of balls with R_{LBi} and a high Young's modulus may be indicated for cases where high fracture loads prevail, and plastic deformation of the loading ball is an issue.

Several simplifications have been made for the construction of Fig. 10. The data for A are related to the contact between a ball and a thick, flat specimen that does not deform globally. In the case of the B3B-test, the contacted surface is concave and under a general compressive equi-biaxial stress. The curvature will increase the contact area in comparisons to the flat surface case and thus decrease the overall magnitude of the contact stress field. The overall compressive equi-biaxial stress state at the loaded surface of the specimen additionally hinders contact cracking, since tensile stresses are relevant for this phenomenon. The limit curves in the presented map can therefore be regarded as conservative estimates.

6.3. Domains of application

As is evident from the plots in Fig. 6, the factor f does not deviate a lot from f_{new}, i.e. the values of f on the ordinate axis, for certain conditions. These conditions are given by the specimen geometry (relative thickness and relative radius), its elastic properties and the applied load. Even though f_{corr} gives the more accurate result for f, it is not necessary to use this lengthy expression in all cases. In order to determine which expression to use, the impact of the correction factors k_1 and k_2 has been investigated for all valid parameter combinations. A combined correction of k_1 and k_2 of 2% has been set as the limit for the application of f_{new}. This means that if $f_{corr}/f_{new} < 0.98$, f_{new} does not sufficiently describe f anymore and f_{corr} has to be utilized instead. For the following graphs and statements, a testing fixture utilizing steel balls with a Young's modulus of 210 GPa and a Poisson's ratio of $\nu = 0.33$ is assumed. This then reduces the possible parameters to R/R_s, t/R_s, E and ν of the specimen as well as the applied load P. To display the limits in a way that is not dependent on the absolute geometry of the specimen, the applied load will be expressed by the maximum applied stress σ (or the measured strength) instead. Fig. 11 depicts the 2%-limit in dependence of R/R_s for exemplary specimens made from glass, zirconia, and alumina with t/R_s
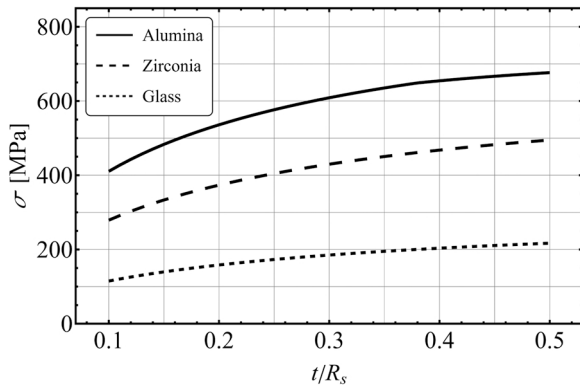
Fig. 12. 2%-Limit for selected specimens with various Young's moduli and Poisson's ratios in dependence of t/R_s.
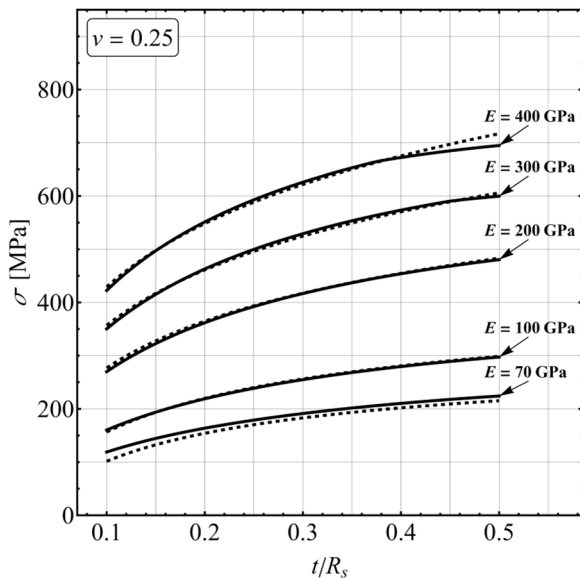

Fig. 13. Comparison of the 2% limit, expressed by the functional expression (dashed), and the curves derived by f_{corr}, for $v = 0.25$.

$= 0.2$. The lines in this Figure display the maximum stress that can be applied to the material before the deviation between f_{corr} and f_{new} is $\geq 2\%$. Therefore, if a specimen exhibits a strength below this line, the simplified evaluation, i.e. Eq. (9), can be utilized. If the strength is higher, then Eq. (21) has to be utilized to accurately determine f.

Fig. 11 shows that R/R_s does not strongly influence the limit. This was found to be true for all other possible configurations of t/R_s, E and v. Therefore, the following graphs will depict the limits only in dependence of t/R_s, E and v. Fig. 12 displays the application limits for typical materials such as glass, zirconia, and alumina.

In order to ensure that the parameter R/R_s can safely be omitted, each datapoint for a specific configuration (t/R_s, E, v) actually represents the lowest value of all R/R_s in its valid range of 1.05–2 for that configuration. This means that the limits shown always assume the worst case in terms of R/R_s, so that no matter what value of R/R_s the tested specimen exhibits, the limit shown might actually be lower than 2%, but never higher. Fig. 3a)-c) of the supplementary material display the limits for more cases, including the special cases discussed in Section 5. An alternative route to convey these limits in a more general form is by providing a functional expression. By setting the Poisson's ratio of the

specimen to a fixed and common value, one function can describe a very broad range of materials and geometries. This has been done for $v = 0.25$, which gives

$$\sigma_{lim} \leq -347 - 497\sqrt{t/R_s} - 0.062\sqrt{E} + 68\sqrt[4]{E \cdot t/R_s} \qquad (23)$$

to describe the limiting strength σ_{Flim} (in MPa) for the application of f_{new} in dependence of t/R_s and E (in MPa). An overview of the accuracy of this expression is shown in Fig. 13. Again, R/R_s was chosen in a way so that it represents the worst-case scenario. Regarding the Poisson's ratio, $v = 0.25$ was chosen since it represents a value close to that of many technical ceramics [31]. A change to a higher Poisson's ratio would shift the curves slightly upwards, while lowering the Poisson's ratio would shift them slightly downwards.

Eq. (23) provides a convenient tool to decide which factor, f_{new} (for $\sigma_F < \sigma_{lim}$) or f_{corr} (for $\sigma_F > \sigma_{lim}$), has to be used to obtain the most accurate result for σ_{max} for a given test geometry or which test geometry is suitable to allow for the use of the simple expression of f_{new}, Eq. (7).

Overall, 3 regimes for the evaluation of f can be defined. If the strength of the material is below the limits displayed in Fig. 13, then the simple functional expression f_{new} (Eq. (9)) can be utilized. If the strength of the material is higher, than the more complex functional expression f_{corr} (Eq. (21)) has to be used. Finally, if the geometry- or material parameters of a specimen are not covered by the given range for f_{new} or f_{corr}, as summarized in Table 8, then individual FEA has to be conducted to determine f. Note that this work has been performed for linear elastic isotropic materials. If the tested specimen exhibits anisotropic behavior or material nonlinearities (such as plastic deformation of the specimen), then neither f_{new} nor f_{corr} should be applied. Again, this would then be a typical case were individual FEA has to be performed.

7. Summary

1) A simplified model of the B3B-test has been utilized to analyze the factor f for a wide range of geometric and material parameters and a new fitted function f_{new}, for the evaluation of the B3B-test is presented.
2) A conversion from square plate specimens to discs with an equivalent diameter D_{eff} for the calculation of f is given. This allows stress evaluation for square plates with the new fitted function f_{new} from 1).
3) The influence of the applied load on the factor f was investigated. Two major effects have been considered separately. First, the increase of contact area between the loading ball and the specimen due to high loads and elastic deformation was investigated. Second, the shift in contact position between the specimen and the support balls due to deflection of the specimen was examined. For each effect, a correction factor that describes the deviation in f is presented.
4) By utilizing these corrections, a range of geometries and material properties can be defined, for which the ideal punctiform solution f_{new} gives an error $< 2\%$ for the calculated maximum stress. Within this range, the simplified evaluation from 1) is sufficient.
5) Cases, which are not included in 4) can be accurately represented by taking the corrections from 3) into account and using $f_{corr} = f_{new}k_1k_2$. Such, the load-dependence of f is given for most practical specimens with strengths up to 2 GPa.
6) Cases, which are not included in 5), have been identified. For these cases, the authors recommend referring to individual solutions by Finite-Element-Analysis.
7) Using the correction factors, the effect of modifications of the suggested test set-up were discussed. It was shown that the use of small support or loading balls or balls with a high Young's modulus has very limited beneficial effects while making the test less practicable. A simple estimation was proposed that showed that contact cracking

at the loading ball can be avoided by using sufficiently thin specimens.
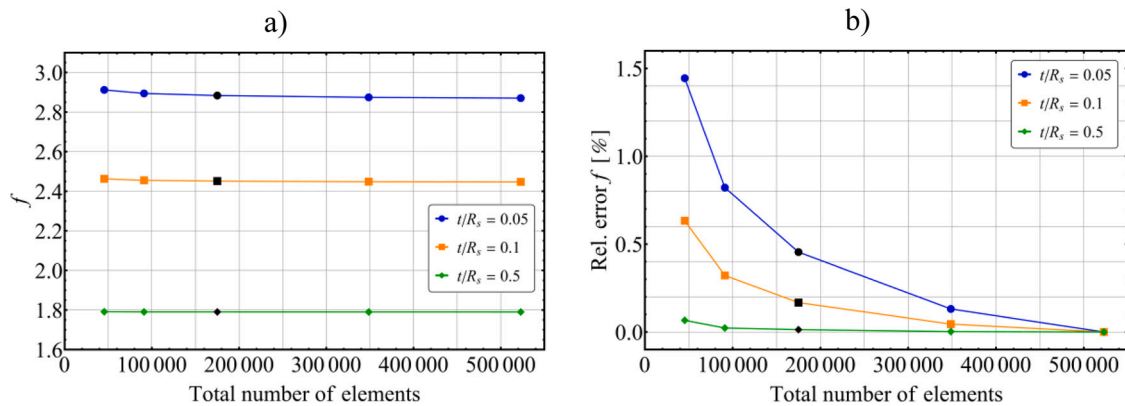
Declaration of Competing Interest

The authors declare that they have no known competing financial interests or personal relationships that could have appeared to influence the work reported in this paper.
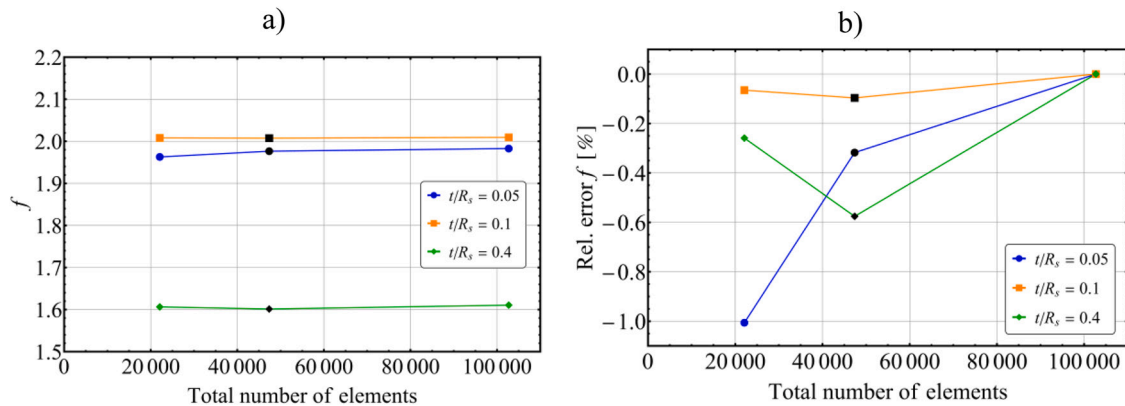
Acknowledgements

Appendix A. – Mesh convergence analysis

In order to obtain the optimum number of elements and mesh configuration for each model, a mesh convergence analysis has been performed. Fig. A1a) shows the absolute factor f for Model 1 in dependence of the total number of elements for three different thicknesses. Fig. A1b) shows the factor f normalized to the value obtained with the highest number of elements. The black markers indicate the mesh utilized in this work.

Since the results of the mesh configuration utilized in this work only display a maximum relative error of 0.5% to the result obtained by approximately tripling the number of elements, it was deemed sufficiently accurate. Model 2 utilizes a similar mesh-density in the central region of maximum stress and is loaded in the same way, hence why no additional mesh convergence analysis was performed for this model.

Due to the different type of loading, the analysis has also been performed for Model 3. As before, Fig. A2a) shows the absolute factor f for three different thicknesses, while Fig. A2b) shows the normalized factor f.

As before, the factor f calculated with the mesh utilized in this work shows a maximum relative error of about 0.6% to the factor f calculated with a model with double the number of elements. For this model, special care was taken to primarily increase the number of elements in the contacting regions of both the balls and the specimen as well as the central tensile loaded regions of the specimen. Due to the iterative nature of the contact analysis, larger deviations between different mesh densities are expected. As soon as the relevant abort criteria are met, the solver is stopped. Since the amount and step size of these iterations changes for each mesh density, final solutions may be just below the abort criteria or well below it. This allows changes of f in both directions, as observed for the thickest specimen in Fig. A2.

Fig. A1. Results for the factor f (a) absolute values, b) normalized values) in the mesh convergence analysis for the model from Section 2.1.1 for a specimen with R/R_s= 1.33, E = 210 GPa, ν= 0.25 and varying thickness. The black markers represent the mesh configuration that was either used directly or slightly modified (in dependence of the specimen's geometry) in this work.

Fig. A2. Results for the factor f (a) absolute values, b) normalized values) in the mesh convergence analysis for the model from Section 2.1.3 for a specimen with R/R_s= 1.05, E = 70 GPa, ν= 0.25 and varying thickness. The black markers represent the mesh configuration that was either used directly or slightly modified (in dependence of the specimen's geometry) in this work.

Appendix B. Supporting information

Supplementary data associated with this article can be found in the online version at doi:10.1016/j.jeurceramsoc.2022.09.047.

References

[1] R. Danzer, Mechanical Performance and Lifetime Prediction, in: Encyclopedia of Adcanced Ceramics, pp. 385–398.

[2] DIN EN 843–1:2008–08: Advanced technical ceramics - Mechanical properties of monolithic ceramics at room temperature - Part 1: Determination of flexural strength; German version EN 843–1:2006, German Institute for Standardisation (Deutsches Institut für Normung), 2008.

[3] D.C. Cranmer, D.W. Richerson (Eds.), Mechanical Testing Methodology for Ceramic Design and Reliability, CRC Press, Taylor & Francis Group, Boca Raton, London, New York, 2018.

[4] ASTM C 1499–05: Test Method for Monotonic Equibiaxial Flexural Strength of Advanced Ceramics at Ambient Temperature, ASTM International, West Conshohocken, PA, 2005.

[5] D. Shetty, A.R. Rosenfield, P. McGuire, G.K. Bansal, W.H. Duckworth, Biaxial flexure test for ceramics, Am. Ceram. Soc. Bull. (1980) 1193–1197.

[6] T.R. Wilshaw, Measurement of tensile strength of ceramics, J. Am. Ceram. Soc. 1968 (1968) 111–112.

[7] D.J. Godfrey, Fabrication, formulation, mechanical properties, and oxidation of sintered Si 3 N 4 ceramics using disc specimens, Mater. Sci. Technol. 1 (1985) 510–515.

[8] R.J. Roark. Roark's Formulas for Stress and Strain, 8th ed..,, McGraw-Hill, New York, 2012.

[9] A.F. Kirstein, R.M. Woolley, Symmetrical bending of thin circular elastic plates on equally spaced point supports, Journal of Research of the National Bureau of Standards, Sect. C Eng. Instrum. 71C (1967).

[10] J.R. Wachtmann Jr, W. Capps, J. Mandel, Biaxial flexure tests of ceramic substrates, J. Mater. (1972) 188–194.

[11] D.J. Godfrey, S. John, Disc flexure tests for the evaluation of ceramic strength, Proceedings 2nd International Conference of Ceramic materials and Components for Engines ,1986, 657–665.

[12] T. Fett, G. Rizzi, E. Ernst, R. Müller, R. Oberacker, A 3-balls-on-3-balls strength test for ceramic disks, J. Eur. Ceram. Soc. 27 (2007) 1–12.

[13] R. Morell, Biaxial flexural strength testing of ceramic materials: a National measurement good practice guide no. 12, Natl. Phys. Lab. (2007).

[14] M. Staudacher, T. Lube, J. Schlacher, P. Supancic, Comparison of biaxial strength measured with the Ball-on-Three-Balls- and the Ring-on-Ring-test, Open Ceram. 6 (2021), 100101.

[15] E. Chicardi, R. Bermejo, F.J. Gotor, L. Llanes, Y. Torres, Influence of temperature on the biaxial strength of cemented carbides with different microstructures, Int. J. Refract. Met. Hard Mater. 71 (2018) 82–91.

[16] H.P.R. Corado, P.H.P.M. Da Silveira, V.L. Ortega, G.G. Ramos, C.N. Elias, Flexural strength of vitreous ceramics based on lithium disilicate and lithium silicate reinforced with zirconia for CAD/CAM, Int. J. Biomater. 2022 (2022) 5896511.

[17] E. Dashjav, M. Gellert, G. Yan, D. Grüner, N. Kaiser, S. Spannenberger, I. Kraleva, R. Bermejo, M.-T. Gerhards, Q. Ma, J. Malzbender, B. Roling, F. Tietz, O. Guillon, Microstructure, ionic conductivity and mechanical properties of tape-cast $Li_{1.5}Al_{0.5}Ti_{1.5}P_3O_{12}$ electrolyte sheets, J. Eur. Ceram. Soc. 40 (2020) 1975–1982.

[18] F. Fleischhauer, R. Bermejo, R. Danzer, A. Mai, T. Graule, J. Kuebler, Strength of an electrolyte supported solid oxide fuel cell, J. Power Sources 297 (2015) 158–167.

[19] L.M. González, E. Chicardi, F.J. Gotor, R. Bermejo, L. Llanes, Y. Torres, Influence of the test configuration and temperature on the mechanical behaviour of WC-Co, Metals 10 (2020) 322.

[20] J.P. Gross, J. Malzbender, R. Schwaiger, Strength assessment of Al2O3 and MgAl2O4 using micro- and macro-scale biaxial tests, J. Mater. Sci. 57 (2022) 7481–7490.

[21] M. Gruber, A. Leitner, I. Kraleva, D. Kiener, P. Supancic, R. Bermejo, Understanding the effect of surface flaws on the strength distribution of brittle single crystals, J. Am. Ceram. Soc. (2018) 5705–5716.

[22] W. Harrer, R. Danzer, P. Supancic, Influence of surface quality on the biaxial strength of silicon nitride, Prakt. Metallogr. Sonderband 42 (2010) 141–146.

[23] M.A. Lodes, F.S. Kachold, S.M. Rosiwal, Mechanical properties of micro- and nanocrystalline diamond foils, Philosophical transactions. Series A, Mathematical, physical, and engineering sciences 373, 2015.

[24] N. Sheth, C. Greenly, R. Bermejo, J.C. Mauro, C.G. Pantano, S.H. Kim, Effects of acid leaching treatment of soda lime silicate glass on crack initiation and fracture, J. Am. Ceram. Soc. 104 (2021) 4550–4558.

[25] A. Börger, P. Supancic, R. Danzer, The ball on three balls test for strength testing of brittle discs: Part II: analysis of possible errors in the strength determination, J. Eur. Ceram. Soc. 24 (2004) 2917–2928.

[26] R. Bermejo, P. Supancic, I. Kraleva, R. Morrell, R. Danzer, Strength reliability of 3D low temperature co-fired multilayer ceramics under biaxial loading, J. Eur. Ceram. Soc. 31 (2011) 745–753.

[27] M. Gruber, I. Kraleva, P. Supancic, J. Bielen, D. Kiener, R. Bermejo, Strength distribution and fracture analyses of LiNbO 3 and LiTaO 3 single crystals under biaxial loading, J. Eur. Ceram. Soc. 37 (2017) 4397–4406.

[28] W. Harrer, R. Danzer, P. Supancic, T. Lube, Influence of the sample size on the results of B3B-Tests, KEM 409 (2009) 176–184.

[29] E. Özkol, A.M. Wätjen, R. Bermejo, M. Deluca, J. Ebert, R. Danzer, R. Telle, Mechanical characterisation of miniaturised direct inkjet printed 3Y-TZP specimens for microelectronic applications, J. Eur. Ceram. Soc. 30 (2010) 3145–3152.

[30] A. Börger, P. Supancic, R. Danzer, The ball on three balls test for strength testing of brittle discs: Stress distribution in the disc, J. Eur. Ceram. Soc. 22 (2002) 1425–1436.

[31] D. Munz, T. Fett, Ceramics: Mechanical Properties, Failure Behaviour, Materials Selection, Springer, Berlin, Heidelberg, 1999.

[32] R. Danzer, P. Supancic, W. Harrer, Der 4-Kugelversuch zur Ermittlung der biaxialen Biegefestigkeit spröder Werkstoffe, Kriegsmann, J. Hrsg Tech. Keram. Werkst. (2009) 1–48.

[33] A.F. Kirstein, W.H. Pell, R.M. Woolley, L.J. Davis, Deflection of centrally loaded thin circular elastic plates on equally spaced point supports, J. Res. Natl Bur. Std. Sect. C Eng. Instrum. 70C (1966) 227–244.

[34] J.D.S. Ramos, S. Fraga, G.F. Vogel, L.G. May, Influence of the geometry of ceramic specimens on biaxial flexural strength: Experimental testing and finite element analysis, Cerâmica 64 (2018) 120–125.

[35] B. Scholtes (Ed.), Forschungsberichte aus dem Institut für Werkstofftechnik Metallische Werkstoffe der Universität Kassel, kassel, University Press, 2012.

[36] H. Hertz, Ueber die Berührung fester elastischer Körper, J. für die reine und Angew. Math. 1882 (1882) 156–171.

[37] T. Fett, E. Ernst, D. Munz, Contact strength measurements of bars under opposite sphere loading, J. Mater. Sci. Lett. 21 (2002) 1955–1957.

[38] F. Auerbach, Absolute Härtemessung, Annalen der Physik 279 (1891) 61–100.

[39] A.C. Fischer-Cripps, Introduction to contact mechanics, 2nd ed., Springer, New York, 2007.

[40] P.D. Warren, Determining the fracture toughness of brittle materials by Hertzian indentation, J. Eur. Ceram. Soc. 15 (1995) 201–207.

[41] J.P.A. Tillett, Fracture of Glass by Spherical Indenters, Proc. Phys. Soc. B 69 (1956) 47–54.

[42] M.T. Laugier, Hertzian indentation of sintered alumina, J. Mater. Sci. 19 (1984) 254–258.

[43] R. Mouginot, D. Maugis, Fracture indentation beneath flat and spherical punches, J. Mater. Sci. 20 (1985) 4354–4376.

[44] S.K. Lee, S. Wuttiphan, B.R. Lawn, Role of microstructure in hertzian contact damage in silicon nitride: I, mechanical characterization, J. Am. Ceram. Soc. 80 (1997) 2367–2381.

[45] J. Wade, S. Ghosh, P. Claydon, H. Wu, Contact damage of silicon carbide ceramics with different grain structures measured by Hertzian and Vickers indentation, J. Eur. Ceram. Soc. 35 (2015) 1725–1736.

[46] T. Lube, J. Dusza, A silicon nitride reference material - a testing program of ESIS TC6, J. Eur. Ceram. Soc. 27 (2007) 1203–1209.

Corrigendum to "The Ball-on-Three-Balls strength test for discs and plates: Extending and simplifying stress evaluation" [J. Eur. Ceram. Soc. 43 (2023) 648–660]

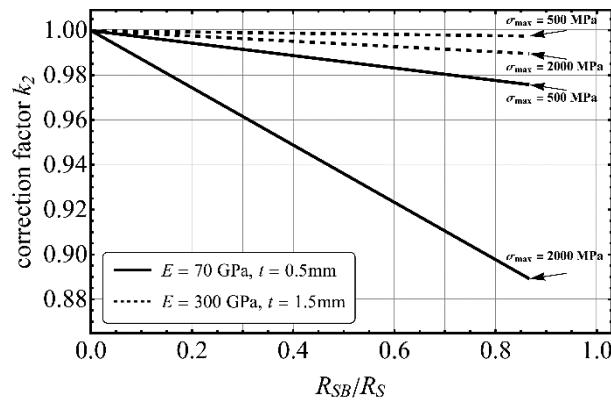In the published article Figure 9 was represented with an incorrectly scaled axis. The corrected figure is:

Figure 9: Correction factor k_2 for exemplary specimens ($R = 6$ mm, $R_S = 5$ mm, $\nu = 0.25$) in dependence of the radius of the support balls (in fractions of the support radius). Through lines represent thin, flexible (glass) specimens ($t = 0.5$ mm, $E = 70$ GPa), dashed lines represent thicker, more typical ceramic specimens ($t = 1.5$ mm, $E = 300$ GPa). Two cases are shown: $\sigma_{max} = 500$ MPa and $\sigma_{max} = 2000$ MPa.

Supplementary material
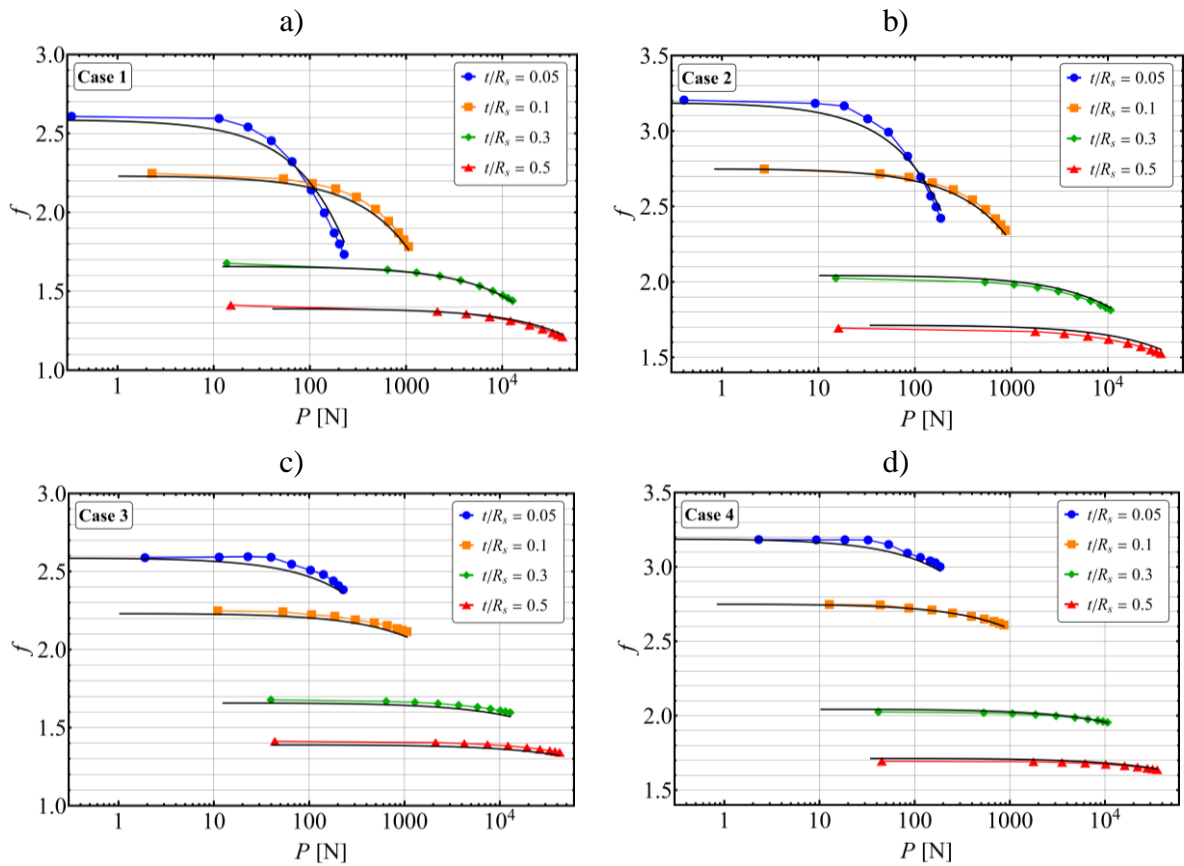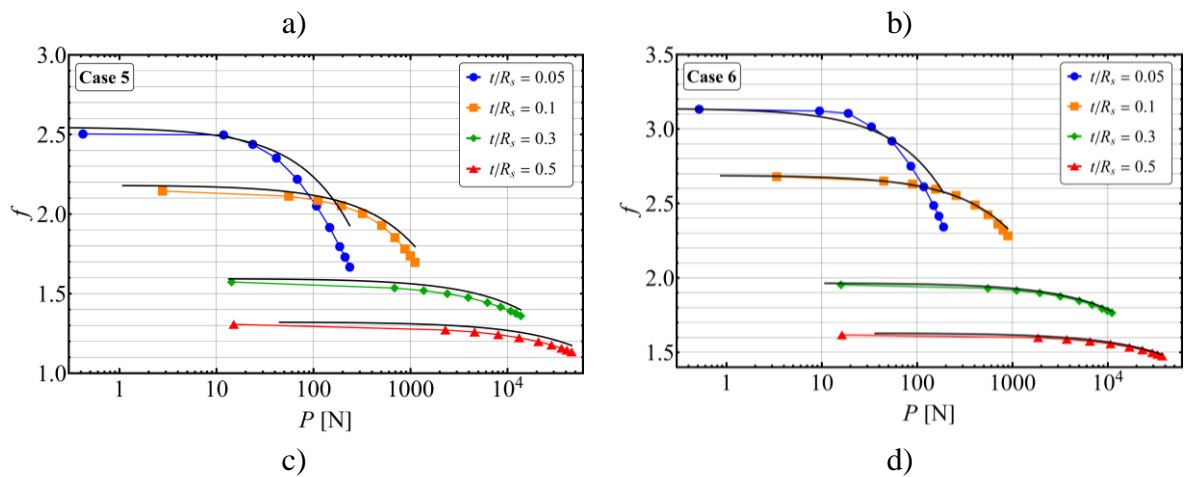
A) Special (extreme) cases for comparison to FEA

a)   b)

c)   d)

Figure 1: Dependence of *f* on the applied load as predicted by FEA and eq. **Fehler! Verweisquelle konnte nicht gefunden werden.**. Figures a), b), c) and d) show the results of specimen 1, 2, 3 and 4, respectively.
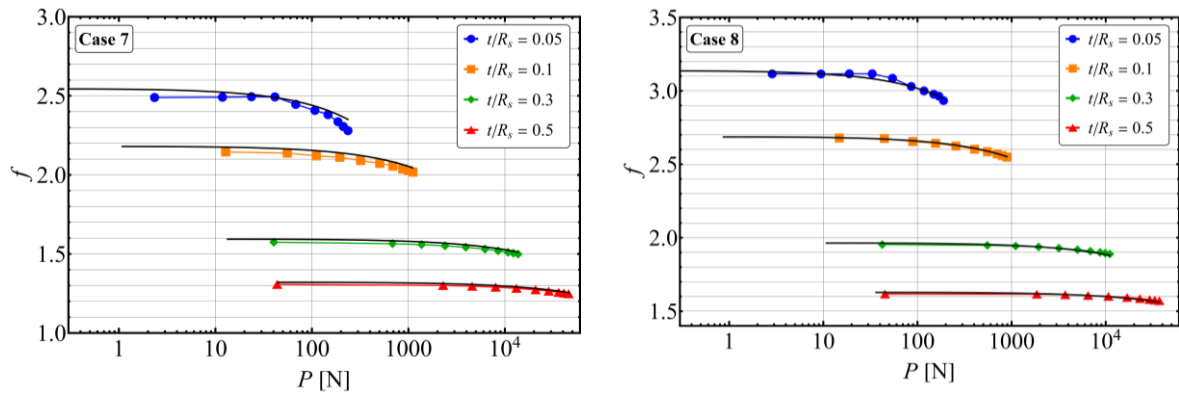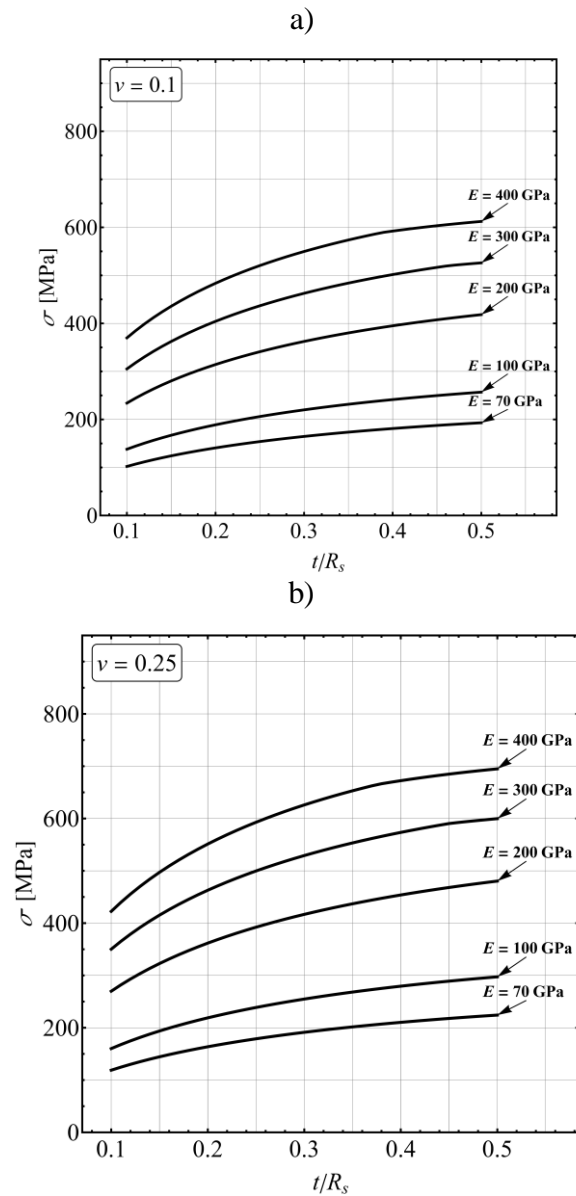
a)   b)

c)   d)

Figure 2: Dependence of *f* on the applied load predicted by FEA and eq. **Fehler! Verweisquelle konnte nicht gefunden werden.**. Figures a), b), c) and d) show the results of specimen 5, 6, 7 and 8, respectively.
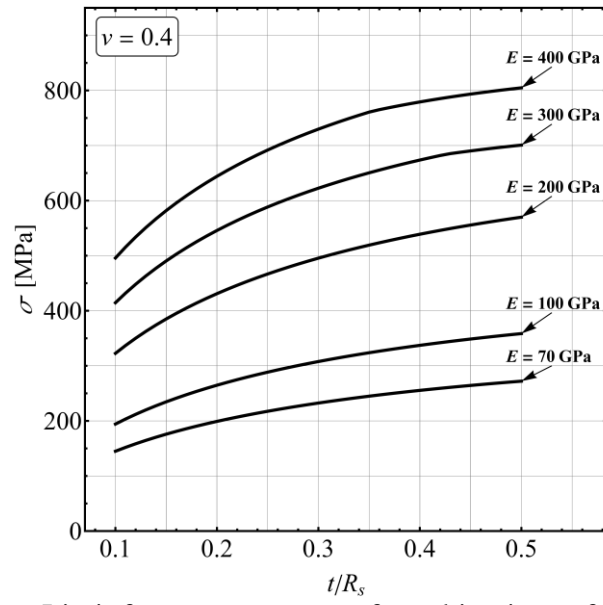
B) 2% limits for f_{corr} for various materials

a)

b)

c)

Figure 3: 2%-Limit for extreme cases of combinations of *E*, *v* and *t/R_s*.